

Two-component dynamics in supercritical CO₂ from inelastic X-ray scattering

Received: 22 December 2025

Accepted: 30 January 2026

Published online: 11 February 2026

Cite this article as: Majumdar A., Sun P., Singleton M. *et al.* Two-component dynamics in supercritical CO₂ from inelastic X-ray scattering. *Sci Rep* (2026). <https://doi.org/10.1038/s41598-026-38697-z>

Arijit Majumdar, Peihao Sun, Madison Singleton, Luigi Paolasini, Alexey Bosak, Alfred Q. R. Baron, Jerome Hastings & Matthias Ihme

We are providing an unedited version of this manuscript to give early access to its findings. Before final publication, the manuscript will undergo further editing. Please note there may be errors present which affect the content, and all legal disclaimers apply.

If this paper is publishing under a Transparent Peer Review model then Peer Review reports will publish with the final article.

ARTICLE IN PRESS

Two-component Dynamics in Supercritical CO₂ from Inelastic X-ray Scattering

Arijit Majumdar¹, Peihao Sun^{2,*}, Madison Singleton³, Luigi Paolasini⁴, Alexey Bosak⁴, Alfred Q.R. Baron⁵, Jerome Hastings⁶, and Matthias Ihme^{1,6,7,*}

¹Mechanical Engineering Department, Stanford University, Stanford, 94305, USA

²Dipartimento di Fisica e Astronomia “Galileo Galilei”, Università degli Studi di Padova, Padova, 35131, Italy

³Applied Physics Department, Stanford University, Stanford, 94305, USA

⁴European Synchrotron Radiation Facility, Grenoble, 38000, France

⁵Materials Dynamics Laboratory, RIKEN SPring-8 Center, Sayo, 679-5148, Japan

⁶SLAC National Accelerator Laboratory, Menlo Park, 94025, USA

⁷Energy Science and Engineering Department, Stanford University, Stanford, 94305, USA

*peihao.sun@unipd.it

*mihme@stanford.edu

ABSTRACT

Supercritical fluids are characterized by unique thermodynamic properties. One of these properties is the existence of two-component dynamics that is associated with distinct low-frequency and high-frequency vibrational responses of the fluid. However, the origin of this behavior remains unknown. By combining inelastic X-ray scattering and molecular dynamics simulations, we show that this behavior can be connected to density heterogeneities arising from molecular clusters. Analyses of measurements and molecular trajectories suggest that the two-component dynamics emerges due to distinct momentum fluctuations of clustered and unbound molecules. This connection between clusters and two-component dynamics highlights the importance of molecular-structural heterogeneities in supercritical fluids, colloids, and condensed-matter systems.

Keywords: Inelastic X-ray scattering; Supercritical fluids; Two-component dynamics; Cluster dynamics; Carbon dioxide

Introduction

Beyond the liquid-vapor critical point, fluids enter the supercritical phase and exhibit strong variations in thermodynamic and transport properties. This makes supercritical fluids (SCFs) relevant for several practical applications, including hydrogen production¹, polymer synthesis² and chemical processing³. Supercritical CO₂, in particular, is important for carbon sequestration since stored CO₂ in the subsurface remains at supercritical conditions⁴. The significance of SCFs thus necessitates a comprehensive understanding of their thermodynamic and transport behavior.

Although there is no liquid-gas phase transition in the supercritical state, the supercritical phase space is often distinguished into liquid-like and gas-like regions based on different criteria, including thermodynamic response functions⁵, microscopic structure⁶, and acoustic response^{7,8}. The transition between liquid-like and gas-like behavior occurs at the Widom line – commonly defined as the locus of extrema in thermophysical properties^{9,10}. Apart from the Widom line, the Frenkel line has been identified as another separatrix between liquid-like and gas-like state¹¹, distinguishing a pure diffusion regime (gas-like) from a diffusion-vibration regime (liquid-like). Different definitions, including velocity

autocorrelation¹², transverse dynamics¹³, and structure factor¹⁴ have been proposed to identify the Frenkel line. Neutron scattering of supercritical N₂ showed the coordination to reach solid-like conditions across the Frenkel line¹⁵. However, the Frenkel line has also been criticized¹⁶, since it does not pass through the critical point and exist at subcritical conditions¹⁷. These studies suggest that there are still unanswered questions related to SCFs.

Recent X-ray and neutron scattering experiments of SCFs have shown the presence of microscopic density heterogeneities^{18–22}. These heterogeneities occur due to the formation of molecular clusters and are most prominent near the Widom line²³. These structural heterogeneities cause several unique features, including increased heat capacity²⁴, enhanced solvation²⁵ as well as a dynamic crossover from ballistic to Brownian motion²⁶. These observations suggest that molecular clusters may have a significant influence on the static and dynamic properties of SCFs.

The existence of microscopic heterogeneities suggests that the dynamics in SCFs may be distinct from homogeneous fluids. Indeed, recent measurements of the current correlation function for supercritical water using inelastic X-ray scattering (IXS)²⁷ showed the existence of two acoustic components, in stark contrast to the single acoustic mode in liquids far away from the critical point²⁸. The two components include a low-frequency (LF) contribution that is consistent with the dynamics of an ideal gas, and a high-frequency (HF) contribution that exhibits liquid-like behavior. Although the two-component dynamics has been linked to the hydrogen-bond (H-bond) in water, several polar and non-polar SCFs that don't form a H-bond network, also display such dynamics²⁹. Therefore, we hypothesize that the two-component dynamics in SCFs emerges due to the existence of molecular clusters and nano-structural heterogeneities, providing a broader physical picture for such dynamics.

In this article, we report results from IXS measurements of supercritical CO₂ (sCO₂). From the measured current correlation function we observe two-component dynamics and demonstrate a strong correlation with molecular clustering using complementary molecular dynamics (MD) simulations. Since the cluster formation is an inherent feature of SCFs²³, our results suggest that the two-component dynamical behavior can represent an universal property of SCFs under equilibrium conditions.

Results

IXS measurements were performed at beamline ID28 of the European Synchrotron Radiation Facility (ESRF). The incident X-ray energy was 21.75 keV, and a Si(11 11 11) backreflection monochromator was used to provide a bandwidth of 1.6 meV (full-width at half maximum, FWHM). The corresponding frequency resolution is 0.38 THz (1 meV \simeq 0.24 THz). Energy scans were performed between -20 meV and 30 meV (Stokes side for positive energy transfer) with nine silicon analyzers, for momentum transfer Q ranging from 0.87 \AA^{-1} to 1.89 \AA^{-1} . Here $Q = 4\pi\sin(\theta)/\lambda$, where λ is the wavelength of the incident X-rays and 2θ is the scattering angle. A detailed discussion of the IXS technique, including a schematic of the experimental setup, can be found in Ref.³⁰. The sample was loaded in a pressure cell, maintained at 88 bar, and the measurements were carried out at temperatures ranging from 292 K to 342 K. Further details about the experimental setup are provided in the Methods section. Note that the critical point of CO₂ is³¹ $P_c = 73.8$ bar and $T_c = 304$ K and henceforth, we report the thermodynamic conditions in reduced coordinates $T_r = T/T_c$ and $P_r = P/P_c$. Figure 1(a) shows the measured experimental conditions in the CO₂ phase diagram. We also show the CO₂ microstructure at $T_r = 0.96$ and $T_r = 1.12$, from MD simulations. At $T_r = 0.96$ (liquid-like condition), the molecules are densely packed into large clusters (cyan colored regions) whereas at $T_r = 1.12$ (gas-like condition), they are more dispersed with few small clusters. The measured thermodynamic conditions cover the liquid-like to gas-like transition region around the Widom line.

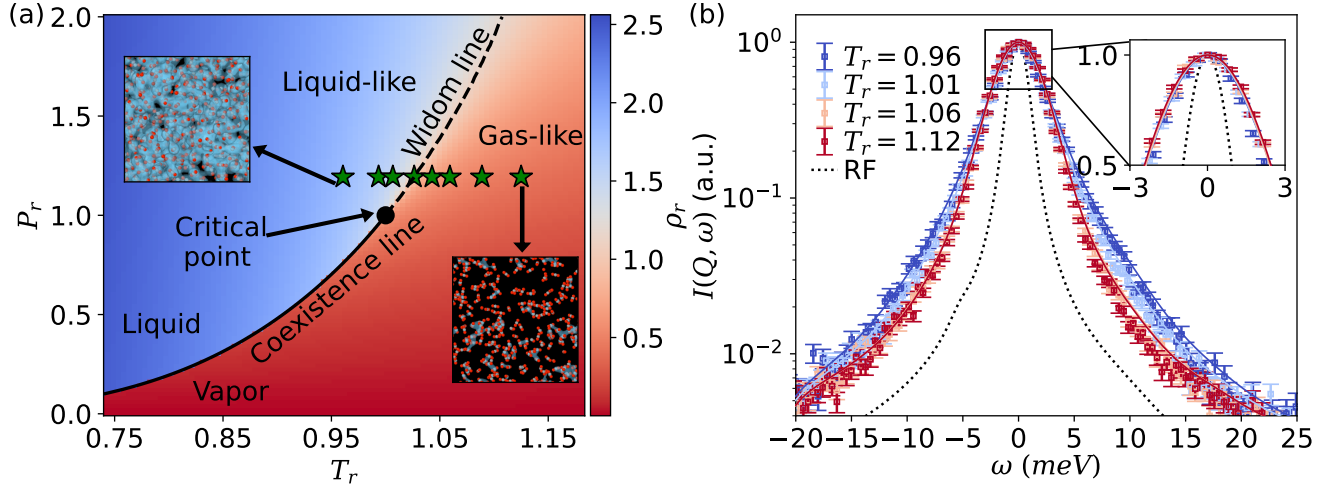


Figure 1. CO₂ phase diagram and intensity from IXS and MD (a) $P - T$ phase diagram of CO₂ with experimental conditions (star symbols). The Widom line is identified as the locus of heat capacity maxima. The insets show the CO₂ molecular arrangement from MD simulations at $P_r = 1.19$, for $T_r = 0.96$ (liquid-like) and $T_r = 1.12$ (gas-like). Carbon and oxygen atoms are shown in grey and red, respectively, with the clusters highlighted in cyan. (b) Intensity $I(Q, \omega)$ vs. frequency ω from IXS (symbols) and MD (lines) for different temperatures at $Q = 1.02 \text{ \AA}^{-1}$. The inset shows the temperature variation in the quasielastic peak of the spectra between $\pm 3 \text{ meV}$.

MD simulations of 8,000 CO₂ molecules were performed in LAMMPS³² with the NPT ensemble and the TraPPE force field³³ at the same reduced pressure and temperature conditions as the experiment. The smallest simulated domain size was 88.3 Å, which covers the measured length scales ($2\pi/Q$). The TraPPE force field was shown to capture thermodynamic properties³⁴ and X-ray scattering measurements²⁶ of sCO₂. See Methods section and Supplementary Note 1 for additional details about the MD simulations and assessments in reproducing thermodynamic properties for CO₂³¹.

In IXS, the measurable quantity is the intensity of the scattered photons $I(Q, \omega)$ ²⁷,

$$I(Q, \omega) = I_0 [R(Q, \omega)] * [B(\omega)S(Q, \omega)], \quad (1)$$

where ω is the frequency, $*$ is the convolution operator, I_0 is an overall intensity factor, $R(Q, \omega)$ is the instrument resolution function (RF) measured from a Plexiglass sample (see Methods section) and $B(\omega)$ is the Bose factor, calculated as $B(\omega) = (\hbar\omega/k_B T)/(1 - \exp\{-\hbar\omega/k_B T\})$. The dynamic structure factor $S(Q, \omega)$ is

$$S(Q, \omega) = \frac{1}{2\pi} \int_{-\infty}^{\infty} \langle \rho(Q, \tau) \rho^*(Q, 0) \rangle \exp\{i\omega\tau\} d\tau, \quad (2)$$

where $\rho(Q, \tau)$ is the electron density at time τ in reciprocal space and $\langle \cdot \rangle$ represents the ensemble average over all microstates of the system. $S(Q, \omega)$ contains information about the dynamics of the molecular motion at a length scale of $2\pi/Q$ and is the primary quantity of interest. $S(Q, \omega)$ can also be calculated from the MD results in the classical limit (see Methods section).

Figure 1(b) shows the intensity $I(Q, \omega)$ from IXS (symbols) and MD (lines) for different temperatures at $Q = 1.02 \text{ \AA}^{-1}$. Results for additional Q values and thermodynamic conditions are provided in the Supplementary Note 1. The spectra in Fig. 1(b) are normalized by $I(Q, 0)$ and the black dotted curve shows

the instrument RF. The MD spectra are calculated from Eq. (1) using $S(Q, \omega)$ from the MD trajectories multiplied by the Bose factor and convolved with the measured RF. Overall, we observe a good agreement between experiments and simulations with the simulated $I(Q, \omega)$ capturing the measured temperature trend. The inset in Fig. 1(b) provides a close-up view of the quasielastic peak between ± 3 meV. With increasing temperature, we observe a decrease in $I(Q, \omega)$ around 5 meV. This frequency corresponds to an acoustic velocity (ω/Q) of 750 m/s, which is the sound speed of sCO₂ at $P_r = 1.19$ and $T_r = 0.84$ (liquid-like condition). Therefore, this reduction in intensity indicates a decrease in the liquid-like behavior of the system. Moreover, the shape of the measured and computed quasielastic peak in the inset of Fig. 1(a), becomes increasingly Gaussian with rise in temperature, indicating an increase in gas-like behavior (see Supplementary Note 2).

To better visualize changes in the acoustic modes and highlight the two-component dynamics, we calculate the longitudinal current-current correlation function $J_l(Q, \omega)$, which, in the classical limit, is related to $S(Q, \omega)$ as²⁸

$$J_l(Q, \omega) = \frac{\omega^2}{Q^2} S(Q, \omega). \quad (3)$$

Obtaining $J_l(Q, \omega)$ from IXS using Eq. (3) typically involves determining $S(Q, \omega)$ using analytic models, such as the memory function^{35,36} or Damped Harmonic Oscillator (DHO) analysis³⁷. While these methods generally work well for liquids, they describe only a single acoustic mode and are thus unable to capture the two-component dynamics in the supercritical region³⁸. See Supplementary Note 3 for a comparison between our measurements and the DHO model. Consequently, following our previous study²⁷, we obtain $J_l(Q, \omega)$ for IXS, without presuming any model, by multiplying $I(Q, \omega)$ with ω^2/Q^2 and subtracting the quasielastic background (see Methods section for more details).

Considering the sum rule ($\int_{-\infty}^{\infty} J_l(Q, \omega) d\omega \propto k_B T$)²⁸, we normalize $J_l(Q, \omega)$ with $k_B T$ to reveal the spectral features. Figure 2(a) shows the normalized $J_l(Q, \omega)$ obtained from experiments (left) and simulations (right) for different temperatures and Q values. There is good qualitative agreement between IXS and MD. In Fig. 2(a), the variation of $J_l(Q, \omega)$ with temperature is similar across different Q values. At low temperature, we observe a peak below 5 meV and a shoulder between 5 and 10 meV. The peaks in the spectra correspond to the gas-like LF components while the shoulders are the liquid-like HF components. Compared to supercritical water²⁷, the frequency separation between LF and HF components is smaller, which we attribute to CO₂ molecules being non-polar and not H-bonded. With increasing temperature, the HF shoulder disappears and the height of the LF peak increases. Therefore, the HF component diminishes and the LF component intensifies as the system transitions from liquid-like to gas-like behavior.

Prior studies of liquids and SCFs have shown increased acoustic speed at nanoscale, referred to as the positive sound dispersion (PSD)^{7,13,39}. The origin of PSD has been related to transverse excitations¹³. It has also been proposed that PSD disappears across the Widom line and marks the transition from liquid-like to gas-like behavior⁷. To determine whether there exists any connection between two-component dynamics and the disappearance of PSD, we quantified the wavelength-dependent sound speed $c(Q)$; $c(Q)$ is calculated as $\omega(Q)/Q$, where $\omega(Q)$ is the location of the maximum of $J_l(Q, \omega)$ ⁷. Figure 2(b) shows $c(Q)$ at $Q = 1.02 \text{ \AA}^{-1}$. Note that $c(Q)$ appears noisy, especially around the Widom line (grey dashed line), since we used the maximum of $J_l(Q, \omega)$ instead of the first moment (see Methods). The black curve in Fig. 2(b) is the adiabatic sound speed of CO₂ from NIST³¹. Within the measured thermodynamic conditions, $c(Q) > c_s$ i.e., PSD exists across the Widom line. This is different from the HF/LF components, undergoing a transition across the Widom line. This implies that the two-component dynamics is independent of the disappearance of PSD⁷.

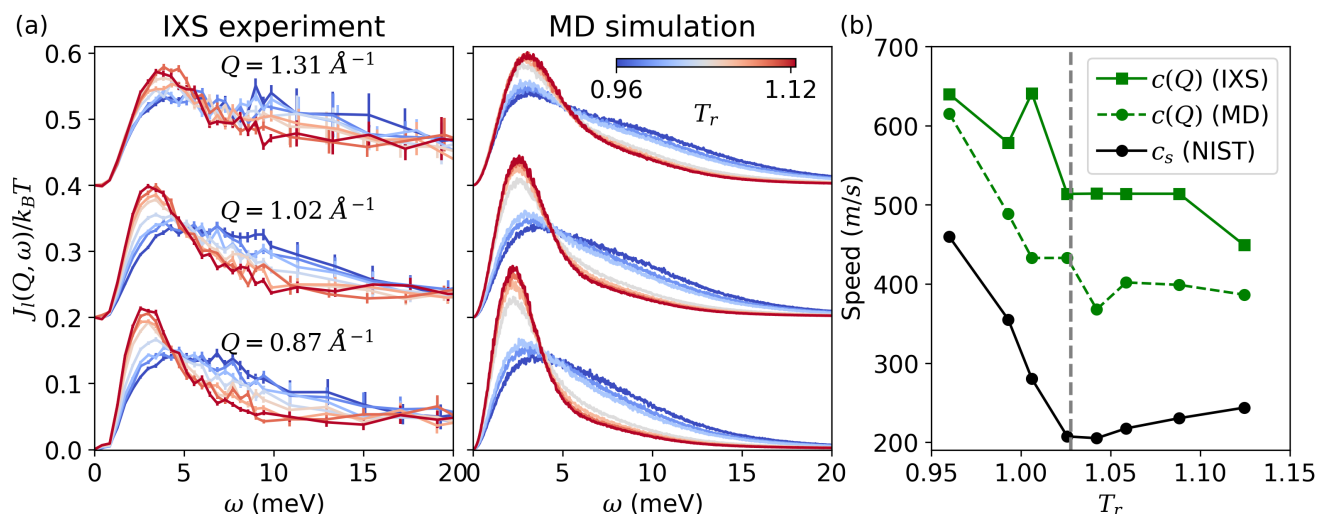


Figure 2. Current correlation function and positive sound dispersion (a) $J_l(Q, \omega)$ from IXS measurements (left panel) and MD simulations (right panel) for reduced temperatures ranging from 0.96 (blue) to 1.12 (red). $J_l(Q, \omega)$ for each Q value is shifted for visual clarity. (b) Wavelength dependent sound speed $c(Q)$, at $Q = 1.02 \text{ \AA}^{-1}$, from IXS and MD as a function of T_r . The grey dashed line is the Widom line. The $c(Q)$ is calculated from the peak location of $J_l(Q, \omega)$ and the results are compared against the adiabatic sound speed c_s from NIST³¹.

To extract the two components in a model-free way, we take an empirical approach and perform non-negative matrix factorization (NMF)^{27,29} on the spectra and decompose $J_l(Q, \omega; P, T)$ as

$$J_l(Q, \omega; P, T) = f(P, T)J_l^{\text{HF}}(Q, \omega) + (1 - f(P, T))J_l^{\text{LF}}(Q, \omega), \quad (4)$$

where $J_l^{\text{LF}}(Q, \omega)$ and $J_l^{\text{HF}}(Q, \omega)$ are the LF and HF components, respectively, and $f(P, T)$ is the fraction of the HF component. The Q dependence of the data is captured by $J_l^{\text{LF}}(Q, \omega)$ and $J_l^{\text{HF}}(Q, \omega)$ while $f(P, T)$ incorporates the $P - T$ dependence. We used all the data in the Q range from 0.87 \AA^{-1} to 1.89 \AA^{-1} to perform the NMF decomposition. More details are given in Supplementary Note 4. Figure 3(a) shows the normalized LF and HF components for three Q values. For these Q values, the LF peaks are below 5 meV or 1.21 THz and the HF peaks are above 6 meV or 1.45 THz.

Detailed physical understanding of these components can be obtained by studying their dispersion relation, i.e., the variation of their mode frequency $\omega_l(Q)$ with Q . We calculate $\omega_l(Q)$ as the first moment of $J_l(Q, \omega)$ (see Methods section for details). The dispersion relation for the HF and LF components from both IXS and MD are shown in Fig. 3(b). The $\omega_l(Q)$ for the LF component follows a linear relation with Q , similar to the acoustic modes in gases²⁸. A linear fit of the data, shown by the black dashed line in Fig. 3(b), gives a phase speed of 477 m/s for IXS and 408 m/s for MD. These values are comparable to the acoustic speed in CO_2 near $T_r = 2.47$ for the measured pressure, which is an extreme gas-like condition³¹.

In contrast, the dispersion relation for the HF component, presented in Fig. 3(b), shows a non-linear trend, where ω_l initially increases with Q and then plateaus around $Q = 1.2 \text{ \AA}^{-1}$. The corresponding length scale (π/Q) is 2.62 \AA and is close to the intermolecular C-O distance in sCO_2 ⁴⁰. This dispersion relation is typically observed in liquids⁴¹ and the plateau occurs as one approaches the boundary of the pseudo-Brillouin zone⁴². Thus, the HF component indicates the presence of liquid-like behavior in SCFs.

Figure 3(c) shows the variation of $f(P, T)$ with T_r at $P_r = 1.19$ for IXS and MD. Here, $f(P, T)$ decreases with increasing T and undergoes a rapid change around the Widom line, marked by the dashed vertical

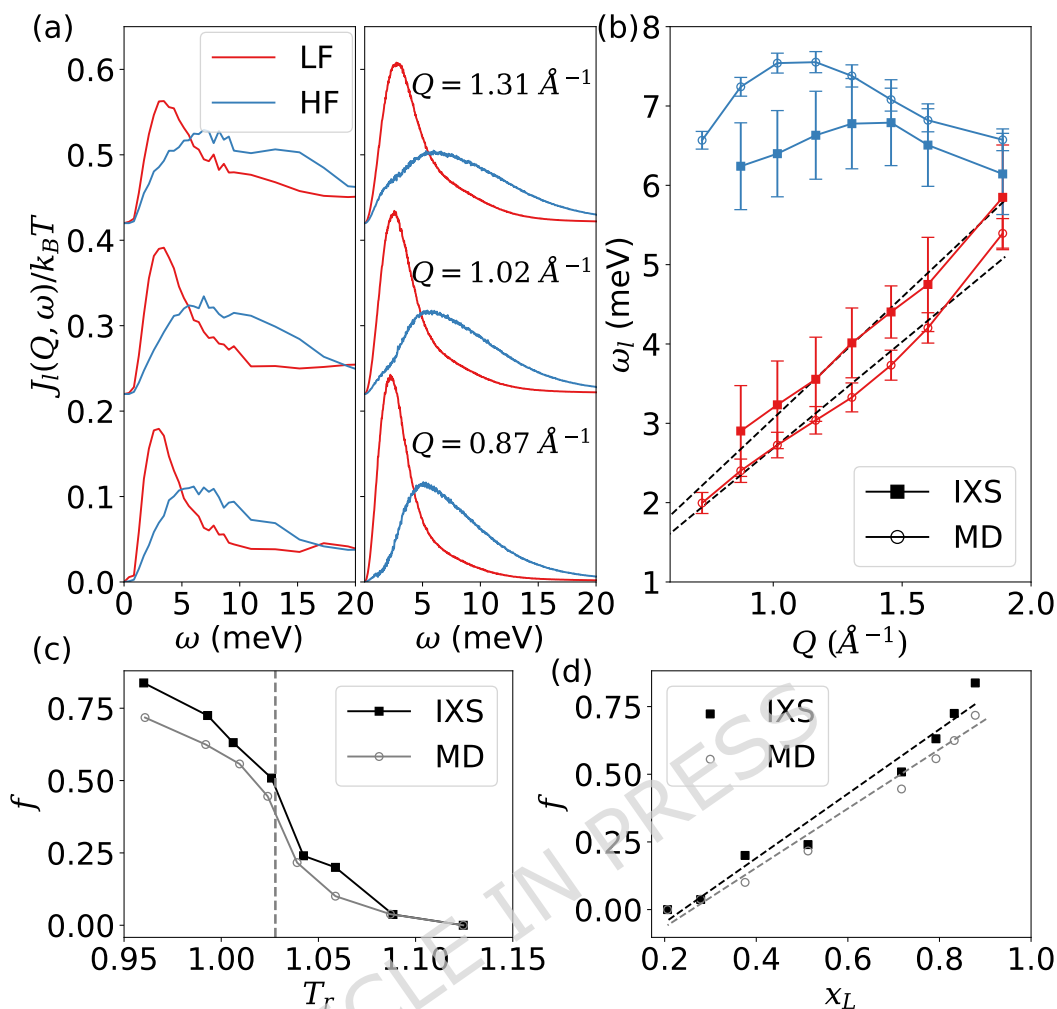


Figure 3. NMF decomposition and connection to molecular clusters. (a) High frequency (HF) liquid-like and low frequency (LF) gas-like components from NMF decomposition of $J_l(Q, \omega)$ from IXS (left) and MD simulation (right). The $J_l(Q, \omega)$ has been vertically shifted for different Q values for visual clarity. (b) Dispersion curve for weighted average frequency from the LF component (red) and HF component (blue). The black dashed lines are linear fits with zero intercepts to the LF component dispersion. (c) Fraction of HF component $f(P, T)$ vs. T_r for IXS and MD. The dashed vertical line shows the location of the Widom line at $P_r = 1.19$. (d) $f(P, T)$ vs. cluster fraction x_L i.e., fraction of molecules inside clusters. Here $f(P, T)$ is from both IXS and MD whereas x_L is obtained from MD only. The dashed lines shows a linear fit between $f(P, T)$ and x_L .

line in Fig. 3(c). Therefore, similar to supercritical H_2O ²⁷, $f(P, T)$ marks the crossover from liquid-like to gas-like region around the Widom line.

Given recent experimental studies, demonstrating the presence of clusters^{26,43}, we hypothesize that the two-component dynamics originates from different dynamical behavior of molecules inside and outside of the clusters. To test this hypothesis, we identify clusters from MD trajectories using Hill's energy criterion^{6,44}: two molecules i and j belong to the same cluster if $K_{i,j} + P_{i,j} < 0$, where $K_{i,j} = Mv_{i,j}^2/4$ is their relative kinetic energy with $v_{i,j}$ the relative velocity and M the molecular mass²³, and $P_{i,j}$ is the potential energy between molecules i and j calculated using the TraPPE force field³³. See Supplementary

Note 5 for details on the cluster analysis.

Determining the influence of clusters on the observed dynamics requires expressing $J_l(Q, \omega)$ in terms of unbound and clustered molecules. Denoting the molecules inside clusters as liquid-like (L) and the unbound molecules as gas-like (G), we can write

$$J_l(Q, \omega) = x_L J_l^L(Q, \omega) + (1 - x_L) J_l^G(Q, \omega), \quad (5)$$

where x_L is the fraction of molecules inside clusters⁶ and $J_l^L(Q, \omega)$ and $J_l^G(Q, \omega)$ are the longitudinal current correlation functions in the liquid-like phase and in the gas-like phase, respectively. The derivation of Eq. (5) is provided in the Supplementary Note 6.

Based on Eqs. (4) and (5) and the liquid-like/gas-like behavior of the HF/LF components, we expect a correlation between x_L and $f(P, T)$. Therefore, we calculate x_L from MD, using cluster analysis, for all measured temperatures and compare it with $f(P, T)$ from both MD and IXS in Fig. 3(d). A linear relationship is observed between $f(P, T)$ and x_L , indicating a strong correlation between the HF component and the molecules inside the clusters. This correlation emphasizes the connection between molecular structure and acoustic dynamics, providing a basis for the two-component dynamics. Specifically, a molecule inside a cluster will experience a higher collision rate compared to an unbound molecule²⁶, leading to frequent momentum exchanges and thus higher-frequency response in $J_l(Q, \omega)$. Since the length scales ($2\pi/Q$) covered in our experiments and simulations are smaller than the average cluster length scale⁴³, the measured dynamics corresponds to the evolution of molecular trajectories in the presence of clusters rather than the coherent cluster dynamics²⁶. Considering the linear correlation between x_L and $f(P, T)$, we can infer that the LF (HF) component in $J_l(Q, \omega)$ arises from the lower (higher) collision rates of molecules outside (inside) clusters.

To quantify the above physical picture, we analyze the effect of clusters on the momentum fluctuations. Since no trajectory is indefinitely inside or outside clusters due to rapid molecular exchange²⁶, we used the cluster residence time, i.e., the time spent by a molecule inside any clusters, to segregate the trajectories. We evaluated the cluster residence time over a time interval of 10 ps, since it covers the slowest measured acoustic modes (see Methods). The distribution of the cluster residence time at $P_r = 1.19$ and $T_r = 1.02$, within 10 ps, is shown in the left panel of Fig. 4(a). Note that the cluster residence time below 5 ps is not shown in Fig. 4(a) since they represent only 0.05 % of the total trajectories. Details about the residence time calculation is provided in the Methods section. Since the thermodynamic condition is close to the Widom line, where a large number of clusters exists, we observe the mean cluster residence time to be 8.4 ps, i.e., molecules on average spend more than 80% of the total trajectory inside clusters. Additionally, a longer cluster residence time can be interpreted as a more liquid-like trajectory.

While vibrational density of states (VDOS)⁴⁵ can be used to quantify momentum fluctuations, the diffusive motion in sCO₂ overwhelms the vibrational features in VDOS (see Supplementary Note 7). To overcome this challenge and quantify the momentum fluctuations, we calculate the spectral vibrational energy $\varepsilon(\omega)$, defined as⁴⁶

$$\varepsilon(\omega) = \left(n_B + \frac{1}{2} \right) \hbar \omega g(\omega), \quad (6)$$

where $n_B = (\exp\{\hbar\omega/k_B T\} - 1)^{-1}$ is the Planck distribution and $g(\omega)$ is the VDOS⁴⁵

$$g(\omega) = \frac{1}{3Nk_B T} \int_{-\infty}^{\infty} \langle \mathbf{v}(t) \cdot \mathbf{v}(t + \tau) \rangle e^{i\omega\tau} d\tau. \quad (7)$$

Here N is the number of CO₂ molecules and $\mathbf{v}(t)$ is their center of mass velocity at time t . We grouped the trajectories based on the cluster residence time given in Fig. 4(a) left panel and calculated $\varepsilon(\omega)$ using

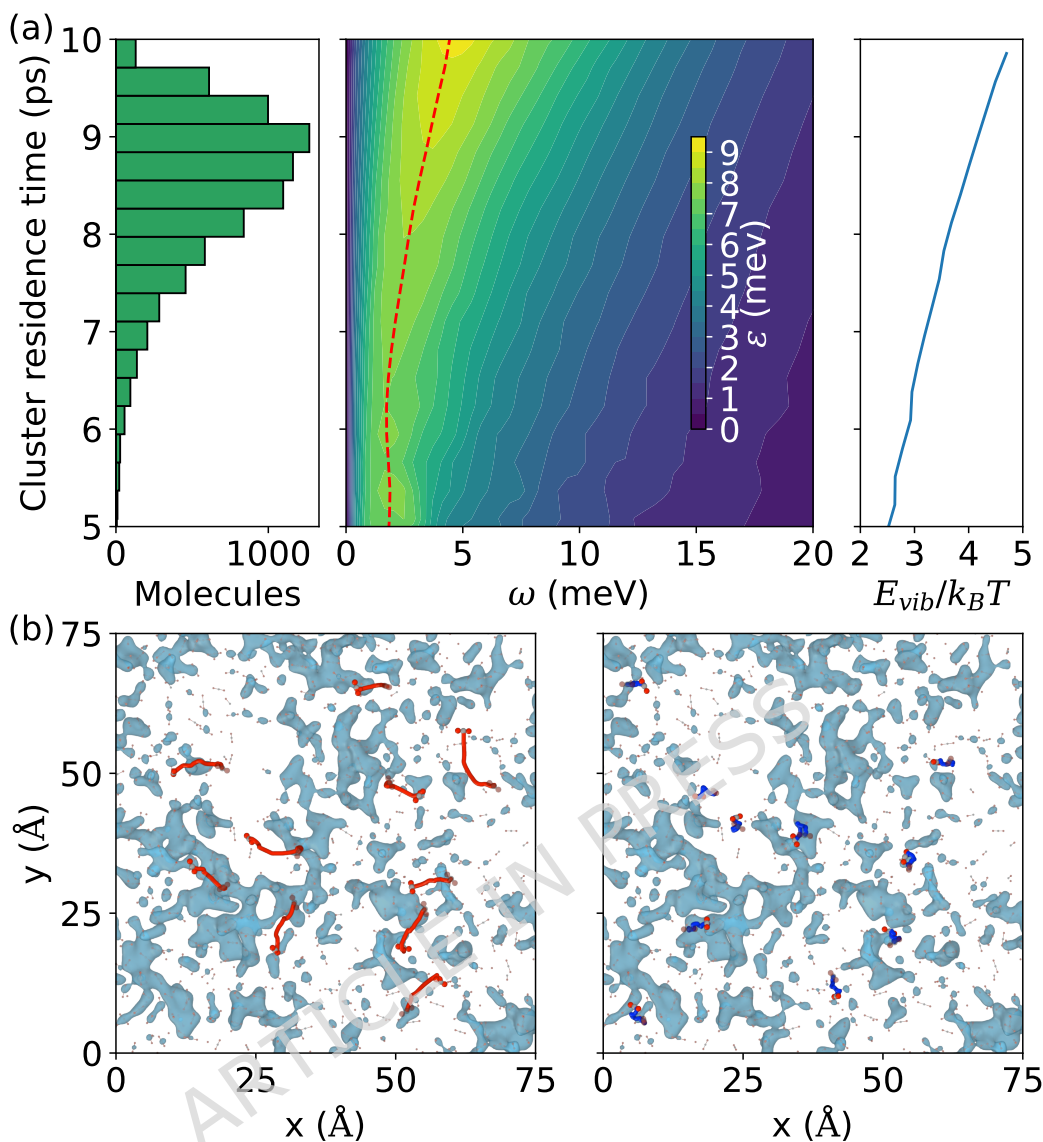


Figure 4. Vibration of liquid-like and gas-like trajectories. (a) Histogram of cluster residence time for all trajectories over 10 ps time interval for $P_r = 1.19$ and $T = 1.02$ (Widom line) in the left panel. Central panel shows the spectral vibrational energy $\varepsilon(\omega)$ as a function of ω and cluster residence time. The red dashed line in the figure shows the peak location in $\varepsilon(\omega)$. Right panel shows the total vibrational energy normalized by $k_B T$. (b) Clusters and trajectories within a $75 \text{ \AA} \times 75 \text{ \AA} \times 20 \text{ \AA}$ region inside the simulation domain. Ten gas-like trajectories (red) and ten liquid-like trajectories (blue) over 5 ps time evolution are highlighted in the left and the right panel, respectively.

Eq. (6) for each group. The VDOS $g(\omega)$ in Eq. (7) was evaluated for trajectories over a 10 ps time interval and ensemble-averaged over 200 ps to obtain converged results. The variation in $\varepsilon(\omega)$ with ω and cluster residence time is shown in Fig. 4(a) middle panel. We observe a peak in $\varepsilon(\omega)$, indicating the dominant vibrational frequency. This vibrational frequency increases with increasing cluster residence time, as shown by the red dashed line. The peak location shifts from 1.86 meV to 4.44 meV with increasing cluster residence time from 5 to 10 ps. Furthermore, the total vibrational energy $E_{vib} = \int_{-\infty}^{\infty} \varepsilon(\omega) d\omega$, shown in the right panel of Fig. 4(a), increases by a factor of two from 5 to 10 ps of cluster residence time. This

increase is close to the ratio of ω_l between HF and LF component, particularly near the pseudo-Brillouin zone boundary ($Q \sim 1.2 \text{ \AA}^{-1}$) (see Fig. 3(b)). These results confirm that the molecules inside the clusters experience higher momentum exchange compared to unbound molecules.

For a physical picture, we show two sets of trajectories from the MD simulations in Fig. 4(b). The left panel in Fig. 4(b) shows trajectories of molecules with 5 ps of average cluster residence time and the right panel shows trajectories with an average cluster residence time of 9 ps. The trajectories in Fig. 4(b) have a time evolution of 5 ps and the molecules in these trajectories have been enlarged for visual clarity. The cyan regions show the instantaneous clusters in the system. The red trajectories in the left panel show large displacements with little change in direction due to fewer intermolecular interactions. Conversely, the blue trajectories in the right panel undergo substantial collision with neighboring molecules. This leads to shorter displacement and more frequent momentum exchanges compared to the red trajectories. These results highlight the lower/higher momentum exchange of molecules outside/inside clusters.

Discussion

The results presented in this work suggest that distinct momentum fluctuations of molecular clusters and unbound molecules are attributed to the two-component dynamics in $J_l(Q, \omega)$. Increase in temperature leads to fewer clusters and in turn weakens the HF component (see Fig. 3(c) and (d)). Since clusters exist in all SCFs²³, the correlation between two-component dynamics and clusters suggests that such dynamics to be an universal phenomenon in single-component SCFs. These results are consistent with the prior study of supercritical water²⁷, where H₂O molecules form H-bonded clusters^{47,48}. The correlation between two-component dynamics and clusters offers a general physical picture for such dynamics in SCFs.

In conclusion, we report inelastic X-ray scattering measurements of sCO₂ across the Widom line at $P = 88$ bars. The measured current correlation function reveals two-component dynamics, which cannot be represented by simple analytical models. The LF and HF components display gas-like and liquid-like behavior, respectively, with crossover around the Widom line. Cluster analysis from complementary MD simulations shows a linear correlation between fraction of HF component and fraction of molecules in clusters, suggesting the two-component dynamics originate from molecular clusters in SCFs. Analyzing the molecular momentum fluctuations showed that the LF/HF components occur due to less/more frequent momentum exchanges of molecules outside/inside clusters. The connection between two-component dynamics and clusters suggests such dynamics to be universal for single-component SCFs at equilibrium. The findings from this work highlight the role of clusters, and more broadly molecular structures, on the nanoscale dynamics in SCFs. The extension of this work to mixtures of different types⁴⁹ would provide opportunities to test the validity of the two-component dynamics for more complex systems.

Methods

Experimental details

The experiments were performed at the ID28 beamline at the European Synchrotron Research Facility. The incident X-rays of 21.75 keV energy were premonochromatized with a Si(1,1,1) and a Si(4,0,0) channel cut crystal. Afterwards, the X-ray was monochromatized using a high-resolution backscattering monochromator with 89.98° Bragg angle and Si(11,11,11) crystals. The X-ray beam was focused onto a spot size of 30 μm diameter using a toroidal mirror.

The sCO₂ was kept in an Inconel 625 pressure cell⁵⁰, confined between two 0.5 mm thick diamond windows with 25 mm sample thickness. The pressure and temperature were monitored using a pressure

gauge and thermocouple. Empty cell measurements were performed to remove the background contribution from the data.

The scattered X-rays from the sample were energy analyzed using an array of nine silicon crystal analyzers mounted on a 7 m long spectrometer arm. Energy scans were performed from -20 meV to $+30$ meV for scattering angles 3.0° and 6.05° to cover a Q -range of $0.87 - 2.0 \text{ \AA}^{-1}$. We used a 4 mm thick Plexiglass sample to measure the resolution function. The minimum signal-to-noise ratio in our measurements, for $\omega \in [-15 \text{ meV}, 15 \text{ meV}]$, is 7.07.

Data analysis

The measured intensity was first corrected to account for the temperature dependence of analyzers using the addIXS software from ESRF⁵¹. Afterwards, we performed background subtraction using the empty cell scattering intensity and reported the intensity in Fig. 1. Additional measured intensities are provided in Supplementary Note 1. The measured RF from the Plexiglass sample was converted into a smooth function using a combination of a Voigt and Lorentzians. This was done to interpolate the RF value at any point within the measured range of frequencies.

To obtain $J_l(Q, \omega)$ from the measured $I(Q, \omega)$, we first scaled the RF to have the same average intensity as $I(Q, \omega)$ within ± 1.5 meV. Then, we subtracted the scaled RF from $I(Q, \omega)$ and multiplied the spectra with ω^2/Q^2 based on Eq. (3) to obtain $J_l(Q, \omega)$. This process of scaling the RF and subtracting from $I(Q, \omega)$ was done to reduce the quasielastic tails in $J_l(Q, \omega)$, which would otherwise lead to violation of the sum rule²⁷.

We calculate the mode frequency from $J_l(Q, \omega)$ as

$$\omega_l(Q) = \frac{\int_0^\infty \omega J_l(Q, \omega) d\omega}{\int_0^\infty J_l(Q, \omega) d\omega}. \quad (8)$$

Evaluating ω_l using Eq. (8) reduces the effect of experimental noise on the dispersion relation compared to obtaining ω_l as the peak frequency. Note that the NMF is a non-unique decomposition. Thus, the absolute value of $\omega_l(Q)$ is less relevant compared to its variation with Q .

MD Simulations

All MD simulations of sCO₂ were performed in LAMMPS³². A cubic domain containing 8,000 CO₂ molecules was simulated with periodic boundary conditions. We used the TraPPE force field³³ due to its acceptable accuracy in predicting X-ray scattering data²⁶. For direct comparisons between experiments and MD simulations, we performed simulations at the same reduced temperature and pressure as the experiments. This removes the effect of the variations in critical point, which is slightly different for the force field ($T_c^{MD} = 306.2$ K and $P_c^{MD} = 77.7$ bar).

The system was equilibrated to the target thermodynamic conditions by performing NPT ensemble simulations for 100 ps with 0.1 fs timestep and Nosé-Hoover thermostat and barostat. The thermostat and barostat have 10 fs and 40 fs of relaxation time, respectively. After equilibration, we performed NVE ensemble simulations of the system for 200 ps and sampled trajectories every 25 fs to have sufficient frequency resolution.

From the MD trajectories, we calculated $S(Q, \omega)$ using Eq. (2), wherein the electron density at time t was calculated as

$$\rho(\mathbf{Q}, t) = \frac{1}{\sqrt{N}} \sum_{j=1}^N b_j(Q) \exp\{i\mathbf{Q} \cdot \mathbf{r}_j(t)\}, \quad (9)$$

where N is the number of atoms, $b(Q)$ is the atomic form factor, $\mathbf{r}_j(t)$ is the atomic coordinates at time t and \mathbf{Q} is the momentum transfer vector. Due to the periodic boundary conditions in the MD simulations, \mathbf{Q} has to be an integer multiple of the reciprocal lattice vector, i.e., $\mathbf{Q} = 2\pi[n_x, n_y, n_z]/L$ with L as the domain size and n_x, n_y and n_z are integers. Since the system is in equilibrium, the ensemble average in Eq. (2) is replaced by temporal averaging over 200 ps. Afterwards, a spherical averaging over \mathbf{Q} with the same magnitude ($|\mathbf{Q}| = Q$) was done to remove any directional effects and compare with experiments. The $J_I(Q, \omega)$ from MD was obtained using Eq. (3).

The cluster residence time was calculated over a time interval of 10 ps. Molecules were categorized as clustered or unbound using Hill's criterion⁴⁴ and the residence time was evaluated as the amount of time a molecule was clustered over the 10 ps duration, i.e., associated with any cluster along its trajectory. The 10 ps interval was chosen since it provides sufficient frequency resolution ($\Delta\omega = 0.41$ meV) and the smallest LF component peak location is around 3 meV (see Fig. 3), which corresponds to a time scale of 8.7 ps. The cluster residence time was ensemble-averaged over the 200 ps simulation using five 10 ps time windows, separated by 30 ps intervals to reduce temporal correlations. We performed a similar ensemble-average for evaluating $\varepsilon(\omega)$ in Eq. (6).

References

1. Correa, C. R. & Kruse, A. Supercritical water gasification of biomass for hydrogen production—review. *J. Supercrit. Fluids* **133**, 573–590 (2018).
2. Kendall, J. L., Canelas, D. A., Young, J. L. & DeSimone, J. M. Polymerizations in supercritical carbon dioxide. *Chem. Rev.* **99**, 543–564 (1999).
3. Brunner, G. Applications of supercritical fluids. *Annu. Rev. Chem. Biomol. Eng.* **1**, 321–342 (2010).
4. Benson, S. M. & Cole, D. R. CO₂ sequestration in deep sedimentary formations. *Elements* **4**, 325–331 (2008).
5. Gallo, P., Corradini, D. & Rovere, M. Widom line and dynamical crossovers as routes to understand supercritical water. *Nat. Commun.* **5**, 5806 (2014).
6. Simeski, F. & Ihme, M. Supercritical fluids behave as complex networks. *Nat. Commun.* **14**, 1996 (2023).
7. Simeoni, G. G. *et al.* The Widom line as the crossover between liquid-like and gas-like behaviour in supercritical fluids. *Nat. Phys.* **6**, 503–507 (2010).
8. Gorelli, F., Santoro, M., Scopigno, T., Krisch, M. & Ruocco, G. Liquidlike behavior of supercritical fluids. *Phys. Rev. Lett.* **97**, 245702 (2006).
9. Xu, L. *et al.* Relation between the Widom line and the dynamic crossover in systems with a liquid–liquid phase transition. *Proc. Natl. Acad. Sci.* **102**, 16558–16562 (2005).
10. Brazhkin, V. V., Fomin, Y. D., Lyapin, A. G., Ryzhov, V. N. & Tsiok, E. N. Widom line for the liquid–gas transition in Lennard-Jones system. *J. Phys. Chem. B* **115**, 14112–14115 (2011).
11. Brazhkin, V. V. *et al.* “liquid-gas” transition in the supercritical region: Fundamental changes in the particle dynamics. *Phys. Rev. Lett.* **111**, 145901 (2013).
12. Yang, C., Brazhkin, V. V., Dove, M. T. & Trachenko, K. Frenkel line and solubility maximum in supercritical fluids. *Phys. Rev. E* **91**, 012112 (2015).

13. Fomin, Y. D., Ryzhov, V. N., Tsiok, E. N., Brazhkin, V. V. & Trachenko, K. Crossover of collective modes and positive sound dispersion in supercritical state. *J. Phys. Condens. Matter* **28**, 43LT01 (2016).
14. Prescher, C. *et al.* Experimental evidence of the Frenkel line in supercritical neon. *Phys. Rev. B* **95**, 134114 (2017).
15. Proctor, J., Pruteanu, C., Morrison, I., Crowe, I. & Loveday, J. Transition from gas-like to liquid-like behavior in supercritical N₂. *J. Phys. Chem. Lett.* **10**, 6584–6589 (2019).
16. Bryk, T. *et al.* Behavior of Supercritical Fluids across the “Frenkel Line”. *J. Phys. Chem. Lett.* **8**, 4995–5001 (2017).
17. Proctor, J. E., Bailey, M., Morrison, I., Hakeem, M. A. & Crowe, I. F. Observation of liquid–liquid phase transitions in ethane at 300 K. *J. Phys. Chem. B* **122**, 10172–10178 (2018).
18. Ishii, R. *et al.* A neutron scattering study of the structure of supercritical carbon dioxide. *Chem. Phys. Lett.* **240**, 84–88 (1995).
19. Nishikawa, K., Tanaka, I. & Amemiya, Y. Small-angle X-ray scattering study of supercritical carbon dioxide. *J. Phys. Chem.* **100**, 418–421 (1996).
20. Morita, T., Nishikawa, K., Takematsu, M., Iida, H. & Furutaka, S. Structure study of supercritical CO₂ near higher-order phase transition line by X-ray diffraction. *J. Phys. Chem. B* **101**, 7158–7162 (1997).
21. Botti, A., Bruni, F., Ricci, M. A. & Soper, A. Neutron diffraction study of high density supercritical water. *J. Chem. Phys.* **109**, 3180–3184 (1998).
22. Pipich, V. & Schwahn, D. Densification of supercritical carbon dioxide accompanied by droplet formation when passing the Widom line. *Phys. Rev. Lett.* **120**, 145701 (2018).
23. Sator, N. Clusters in simple fluids. *Phys. Rep.* **376**, 1–39 (2003).
24. Fan, J., Ly, N. & Ihme, M. Heterogeneous cluster energetics and nonlinear thermodynamic response in supercritical fluids. *Phys. Rev. Lett.* **133**, 248001 (2024).
25. Maddox, M. W., Goodyear, G. & Tucker, S. C. Origins of atom-centered local density enhancements in compressible supercritical fluids. *J. Phys. Chem. B* **104**, 6248–6257 (2000).
26. Majumdar, A. *et al.* Direct observation of ultrafast cluster dynamics in supercritical carbon dioxide using X-ray photon correlation spectroscopy. *Nat. Commun.* **15**, 10540 (2024).
27. Sun, P., Hastings, J. B., Ishikawa, D., Baron, A. Q. R. & Monaco, G. Two-component dynamics and the liquidlike to gaslike crossover in supercritical water. *Phys. Rev. Lett.* **125**, 256001 (2020).
28. Boon, J. P. & Yip, S. *Molecular Hydrodynamics* (Courier Corporation, 1991).
29. Sun, P., Hastings, J., Ishikawa, D., Baron, A. Q. R. & Monaco, G. Universal two-component dynamics in supercritical fluids. *J. Phys. Chem. B* **125**, 13494–13501 (2021).
30. Baron, A. Q. R. High-resolution inelastic x-ray scattering I: Context, spectrometers, samples, and superconductors. In Jaeschke, E., Khan, S., Schneider, J. R. & Hastings, J. B. (eds.) *Synchrotron Light Sources and Free-Electron Lasers: Accelerator Physics, Instrumentation and Science Applications*, 2131–2212 (Springer, Cham., 2020).

31. Lemmon, E. W., Bell, I. H., Huber, M. L. & McLinden, M. O. Thermophysical properties of fluid systems. In Linstrom, P. J. & Mallard, W. G. (eds.) *NIST Chemistry WebBook, NIST Standard Reference Database Number 69* (National Institute of Standards and Technology, Gaithersburg MD, 20899, 2025).
32. Thompson, A. P. *et al.* LAMMPS-a flexible simulation tool for particle-based materials modeling at the atomic, meso, and continuum scales. *Comput. Phys. Commun.* **271**, 108171 (2022).
33. Potoff, J. J. & Siepmann, J. I. Vapor-liquid equilibria of mixtures containing alkanes, carbon dioxide, and nitrogen. *AIChE J.* **47**, 1676–1682 (2001).
34. Aimoli, C. G., Maginn, E. J. & Abreu, C. R. A. Force field comparison and thermodynamic property calculation of supercritical CO₂ and CH₄ using molecular dynamics simulations. *Fluid Ph. Equilib.* **368**, 80–90 (2014).
35. Bencivenga, F. *et al.* High-frequency dynamics of liquid and supercritical water. *Phys. Rev. E* **75**, 051202 (2007).
36. Monaco, G., Cunsolo, A., Ruocco, G. & Sette, F. Viscoelastic behavior of water in the terahertz-frequency range: An inelastic x-ray scattering study. *Phys. Rev. E* **60**, 5505 (1999).
37. Ishikawa, D. & Baron, A. Q. R. Interaction of acoustic and quasi-elastic modes in liquid water on nanometer length scales. *J. Phys. Soc. Jpn.* **90**, 083602 (2021).
38. Sun, P. *Molecular Dynamics of Supercritical Fluids*. Ph.D. thesis, Stanford University (2021).
39. Sampoli, M., Ruocco, G. & Sette, F. Mixing of longitudinal and transverse dynamics in liquid water. *Phys. Rev. Lett.* **79**, 1678 (1997).
40. Bolmatov, D., Zav'Yalov, D., Gao, M. & Zhernenkov, M. Structural evolution of supercritical CO₂ across the Frenkel line. *J. Phys. Chem. Lett.* **5**, 2785–2790 (2014).
41. Giordano, V. M. & Monaco, G. Fingerprints of order and disorder on the high-frequency dynamics of liquids. *Proc. Natl. Acad. Sci.* **107**, 21985–21989 (2010).
42. Scopigno, T., D'astuto, M., Krisch, M., Ruocco, G. & Sette, F. Observation of Umklapp processes in noncrystalline materials. *Phys. Rev. B* **64**, 012301 (2001).
43. Muhunthan, P. *et al.* A self-consistent analysis of cluster morphology in supercritical carbon dioxide from small angle x-ray scattering. *Chem. Phys. Lett.* 142190 (2025).
44. Hill, T. L. Molecular clusters in imperfect gases. *J. Chem. Phys.* **23**, 617–622 (1955).
45. Simdyankin, S. I., Taraskin, S. N., Dzugutov, M. & Elliott, S. R. Vibrational properties of the one-component σ phase. *Phys. Rev. B* **62**, 3223 (2000).
46. Kittel, C. & McEuen, P. *Introduction to Solid State Physics* (John Wiley & Sons, 2018).
47. Kalinichev, A. G. Molecular simulations of liquid and supercritical water: Thermodynamics, structure, and hydrogen bonding. *Rev. Mineral. Geochem.* **42**, 83–129 (2001).
48. Boero, M., Terakura, K., Ikeshoji, T., Liew, C. C. & Parrinello, M. Hydrogen bonding and dipole moment of water at supercritical conditions: A first-principles molecular dynamics study. *Phys. Rev. Lett.* **85**, 3245 (2000).
49. Rowlinson, J. S. & Swinton, F. L. *Liquids and Liquid Mixtures* (Butterworth-Heinemann, 2013).
50. Mattenet, M. *et al.* An X-Ray Thermo-Pressure Cell For Carbon Dioxide. In *AIP Conference Proceedings*, vol. 1234, 111–114 (American Institute of Physics, 2010).

51. Walters, A. C. *Using X-ray and neutron scattering to study the dynamics of low-dimensional systems*. Ph.D. thesis, University College London (2009).
52. Majumdar, A. *et al.* Database for heterogeneity induced universal two-component dynamics in supercritical fluids, DOI: <https://doi.org/10.25740/sj299gg3375> (2025).

Funding Declaration

Financial support from the U.S. Department of Energy, Office of Science under DOE (BES) Awards DE-SC0022222 and DE-SC0026165 (A.M. and M.I.) is gratefully acknowledged.

Author Contributions

A.M.: Data curation, Formal analysis, Investigation, Methodology, Software, Visualization, Writing – original draft, Writing – review & editing; P.S.: Data curation, Formal analysis, Investigation, Methodology, Writing – review & editing; M.S.: Data curation, Formal analysis, Investigation, Methodology, Software, Writing – review & editing; L.P.: Investigation, Methodology, Resources, Writing – review & editing; A.B.: Investigation, Methodology, Resources, Writing – review & editing; A.Q.R.B.: Formal analysis, Investigation, Methodology, Software, Writing – review & editing; J.H.: Investigation, Methodology, Resources, Project administration, Supervision, Writing – review & editing; M.I.: Conceptualization, Investigation, Methodology, Resources, Funding acquisition, Project administration, Supervision, Writing – review & editing

Competing Interests

The authors declare no competing interest.

Data Availability

The data supporting the findings of the study are included in the main text and supplementary information files. Source data have been deposited in the Supplementary Material and Stanford Digital Repository⁵². Additional data are available from the corresponding author upon request.

Code Availability

The MD simulations were performed with the open-source software LAMMPS (release date 8 April, 2021). Code for the analysis of the experimental data is available from the corresponding author upon request.